scientific reports

OPEN

A novel chronostratigraphic framework for the Aptian–Albian paleoclimate events

João M. F. Ramos[1,2]✉, Jairo F. Savian[1,3], Daniel R. Franco[4], Milene F. Figueiredo[5], Carolina G. Leandro[3], Rodolfo Coccioni[6], Fabrizio Frontalini[7], Nicola Casadei[7], Hironao Matsumoto[8,9], Leonardo R. Tedeschi[10], Luigi Jovane[11] & Ricardo I. F. Trindade[12]

The Aptian–Albian interval was marked by paleoclimatic changes encompassing volcanic events and monsoonal activity of which the precise timing were not well-defined. This study presents a ~ 20 Myr cyclostratigraphic framework and provides an extended astronomical timescale using magnetic susceptibility and anhysteretic remanent magnetization datasets from the Poggio le Guaine core (Umbria–Marche Basin, Italy). Using astronomical tuning, we infer new age constraints and timespans for: (1) the Aptian and Albian stages; (2) the magnetic polarity Chron M0r; (3) the Oceanic Anoxic Events; (4) bioevents and, (5) Cretaceous oceanic red beds. These results enhance our understanding of the interplay between paleoclimatic and biotic processes in the Early Cretaceous. This study establishes a new chronostratigraphic framework for the Aptian–Albian—the most comprehensive to date in terms of resolution, integration with other geochronological methods, and temporal coverage— offering new insights into bio-chemical–geomagnetic interactions and helping refine the Geological Time Scale.

The Aptian–Albian interval (121.4 to 100.5 million years ago) was characterized by significant tectonic and paleoclimatic changes that profoundly influenced global sea levels and oceanic conditions[1–9]. Continental breakup during this period drove the formation of new oceanic ridges and accelerated seafloor spreading, leading to shallower, potentially anoxic oceans and elevated global sea levels[10,11].

The Cretaceous experienced the largest long-term eustatic fluctuations of the entire Phanerozoic, largely controlled by the increasing ridge volume associated with the opening of the South Atlantic and Southern Ocean basins[11,12]. This tectonic activity contributed to a sustained sea-level rise, primarily driven by changes in ocean basin volume and enhanced seafloor spreading linked to the development of these nascent ocean basins[13]. Superimposed on this long-term trend were pronounced short-term fluctuations, especially evident at the Aptian–Albian boundary, reflecting a complex interplay of processes and a shift in the dominant controls on sea-level change—from tectonic drivers to astronomically forced climate variations[11,14].

Concurrently, the interval witnessed major paleoclimatic shifts linked to volcanism, monsoonal activity, and changes in ocean circulation[1–9]. These environmental changes induced rhythmic black shale deposition, abrupt oceanic redox fluctuations, alterations in precipitation and runoff that affected halocline and thermocline stratification, foraminiferal turnovers, and episodic hyperthermal and cooling events within an overall greenhouse climate[15]. However, the precise timing and duration of these events remain poorly constrained, fueling debate over their causes and global impacts[16–19]. This uncertainty is further compounded by imprecise

[1]Programa de Pós-Graduação em Geociências, Universidade Federal do Rio Grande do Sul, Av. Bento Gonçalves 9500, Porto Alegre, RS 91501-970, Brazil. [2]Petrobras Petróleo Brasileiro S.A, Exploration, Rio de Janeiro, Av. Henrique Valadares 28, Rio de Janeiro, RJ 20231-030, Brazil. [3]Instituto de Geociências, Universidade Federal do Rio Grande do Sul, Av. Bento Gonçalves 9500, Porto Alegre, RS 91501-970, Brazil. [4]Coordenação de Geofísica, Observatório Nacional, R. General José Cristino, 77, Rio de Janeiro, RJ 20921-400, Brazil. [5]Centro de Pesquisas e Desenvolvimento Leopoldo Américo Miguez de Mello, Petrobras Petróleo Brasileiro S.A, Avenida Horácio Macedo 950, Rio de Janeiro 21941-915, Brazil. [6]Università degli Studi di Urbino Carlo Bo, 61029 Urbino, Italy. [7]Dipartimento di Scienze Pure e Applicate, Università degli Studi di Urbino "Carlo Bo", Campus Scientifico, Località Crocicchia, 61029 Urbino, Italy. [8]Institute of Life and Environmental Sciences, University of Tsukuba, 1-1-1, Tennodai, Tsukuba, Ibaraki 305-8572, Japan. [9]Japan Agency for Marine-Earth Science and Technology, Yokosuka, Japan. [10]Petrobras Petróleo Brasileiro S.A, LIBRA, Rio de Janeiro, Av. Henrique Valadares 28, Rio de Janeiro, RJ 20231-030, Brazil. [11]Instituto Oceanográfico, Universidade de São Paulo, Praça do Oceanográfico 191, São Paulo, SP 05508-120, Brazil. [12]Departamento de Geofísica, Instituto de Astronomia, Geofísica e Ciências Atmosféricas, Universidade de São Paulo, Rua do Matão 1226, São Paulo, SP 05508-090, Brazil. ✉email: j.m.f.ramos@petrobras.com.br

age models and data gaps in Cretaceous records, which limit detailed understanding of climate dynamics during this critical period.

During the Aptian, the proximity of continents caused unstable circulation in the Tethys Ocean, with frequent oceanic oscillations on a 10^2 kyr timescale[9]. This led to four oceanic anoxic events—OAEs (1a, 1b, 1c, and 1d) that denote intervals of episodic burial of organic-rich sediments (i.e., black shale layers) under oxygen-deficient bottom waters[7,17,20]. The early Aptian OAE 1a, also known as the Selli event, was the most prominent (i.e., ca. 1-Myr-long-lasting event[16,17]) event and was associated with Large Igneous Provinces (LIP) volcanism, as revealed by the osmium isotope record[8,21]. The OAE 1b was characterized by a ca. 2.84 Myr prolonged period of organic carbon burial[19] and encompassed multiple short-duration sub-events resulting from the combination of a warm climate (driven by volcanic CO_2 emissions), heavy precipitation, and intense weathering, all of which amplify orbital forcing[22]. The early-late Albian OAE 1c and late Albian OAE 1d were supra-regional marine anoxic events[8] of limited magnitude, affecting the North Atlantic and proto-Atlantic Ocean.

Despite an overall warming trend, a global cooling event known as the "cold snap" occurred in the late Aptian[18,23]. The end of this period is marked by a foraminiferal turnover[24] and one of the most pronounced breaks in the maximum magnitudes of short-term sea-level variation[14], suggesting a major shift in the ocean–atmosphere system. These variations indicate a complex interplay of processes and suggest a shift in the dominant controls on global sea-level change—from tectonically driven mechanisms towards those modulated by astronomically forced climate variations[11].

We examine the Poggio le Guaine (PLG) core, a key sedimentary record for Cretaceous biostratigraphy[20] (Fig. 2). This core from the Umbria-Marche Basin (Tethys Ocean)[7,20] provides a comprehensive record of OAEs, organic-rich beds, and seven Cretaceous Oceanic Red Beds (CORBs) intervals (Fig. 2a). The PLG core records changes in ocean circulation from the period preceding the opening of the South Atlantic to the establishment of full connectivity between the South and North Atlantic via the equatorial seaway[25] (Fig. 1). This circulation shift, observed near the record's top, marks a transition to more stable conditions with a well-defined thermocline and enhanced currents[9]. The bioevents, isotopic data, and Chron M0r[26] help develop a refined reference age model[3,8,27,28]. The PLG core also records key biohorizons: the *Globigerinelloides aptiensis* zone at the base of the Aptian, *Leupoldina cabri* zone (OAE 1a), *Microhedbergella miniglobularis* zone (foraminiferal turnover), *Microhedbergella renilaevis* (top of the Aptian), *Biticinella breggiensis* zone (OAE 1c), and *Thalmanninella globotruncanoides* zone marking the Albian-Cenomanian boundary[7,20] (Fig. 2a). High-resolution paleoclimatic proxies from the PLG core enable precise positioning of these events within the Geological Time Scale (GTS)[1].

This study presents a new astronomically tuned age model using magnetic susceptibility (MS) and anhysteretic remanent magnetization (ARM) as proxies for the PLG core[7,20], which spans from the base of the Aptian stage to the base of the Cenomanian[18,20,26], (Fig. 2b,c). The astrochronology age model was anchored with the Chron M0r[26,32] and to the absolute dating of Vöhrum's tuff[33,34], transferred via isotope correlation from the original location to the PLG core[22]. The astrochronological study presented here offers an opportunity to develop a high-resolution age model for a ~ 20 Myr-long interval of continuous sedimentary record—from OAE 1a to OAE 1d—using high-resolution magnetic proxies. We also determine the ages of CORBs and biostratigraphic events along this interval. Furthermore, by converting spatial (meters) to temporal domain (million years) using orbitally influenced proxies, we can convert the carbon ($\delta^{13}C$) stable isotope profile to the time domain and estimate the durations of volcanic events, as constrained by the $^{187}Os/^{188}Os$ ratios[8], (Fig. 2d,e). Our results provide an astronomically tuned, high-definition stratigraphic reference record of global climate evolution for the Aptian-Albian interval.

Results and discussion

Integrated stratigraphy and biozones

White cherty limestone, cyclically intercalated with a few centimeter-thick black shale layers of the Maiolica Fm. occurs at the base of the core (Fig. 2a). The most prominent organic-rich interval, the Selli Level, is found between 89.24 and 91.19 m and represents the sedimentary expression of OAE 1a[18,26]. Additional black shale layers between 88–88.2 and 79.31–79.37 m correspond to the Wezel and Fallot Levels, respectively, which have exclusively been reported from the Tethyan region[18].

An organic-rich marker bed, the Jacob Level (67.44–67.52 m), marks the onset of OAE 1b (Fig. 2). This OAE is characterized by several prominent organic-rich intervals, including the sub-events designated as the Kilian (62.64–63.02 m), Monte Nerone (57.07–60.01 m), Urbino/Paquier (54.63–54.88 m), and Leenhardt (52.97–53.26 m) Levels[22]. The top of the Aptian interval, marked by the lowest occurrence (LO) of *Microhedbergella renilaevis*[1], is set at 63.40 m.

An approximately 3-m-thick interval (24.74–27.77 m), known as the Amadeus Segment[24,28], lies within the Albian interval and represents OAE 1c (Fig. 2). The regional sedimentary expression of OAE 1d[35] is at the top of the PLG core. Additionally, within the Scaglia Bianca Fm.[36], the Pialli/Breistroffer Level (0.95–4.91 m) is close to the boundary with the Cenomanian stage and exhibits a cyclic character influenced by orbital forcing[27].

The succession of primary planktonic foraminiferal bioevents allowed the subdivision of the section into the following zones and subzones (in stratigraphic order): *Globigerinelloides aptiensis* during the Barremian–Aptian transition, *Leupoldina cabri*, *Globigerinelloides ferreolensis*, *Globigerinelloides algerianus*, *Hedbergella trocoidea*, *Paraticinella rohri*, and *Microhedbergella miniglobularis* in the Albian (Fig. 2). The Aptian–Albian boundary is marked by the FO of *Microhedbergella renilaevis*[1]. The Albian succession encompasses the *Microhedbergella rischi*, *Ticinella primula*; *Ticinella praeticinensis*, *Pseudothalmanninella subticinensis* (the last two forming the *Biticinella breggiensis*), *Pseudothalmanninella ticinensis Parathalmanninella appenninica* and ending with *Thalmanninella globotruncanoides*, which marks the top of the Albian[29].

The calcareous nannofossil zones[30] include *Chiastozygus litterarius* (NC6), *Rhagodiscus angustus* / *Eprolithus floralis* (NC7), *Paraticinella columnata* (subcircular) in the Aptian, *Paraticinella columnata* (circular, NC8A),

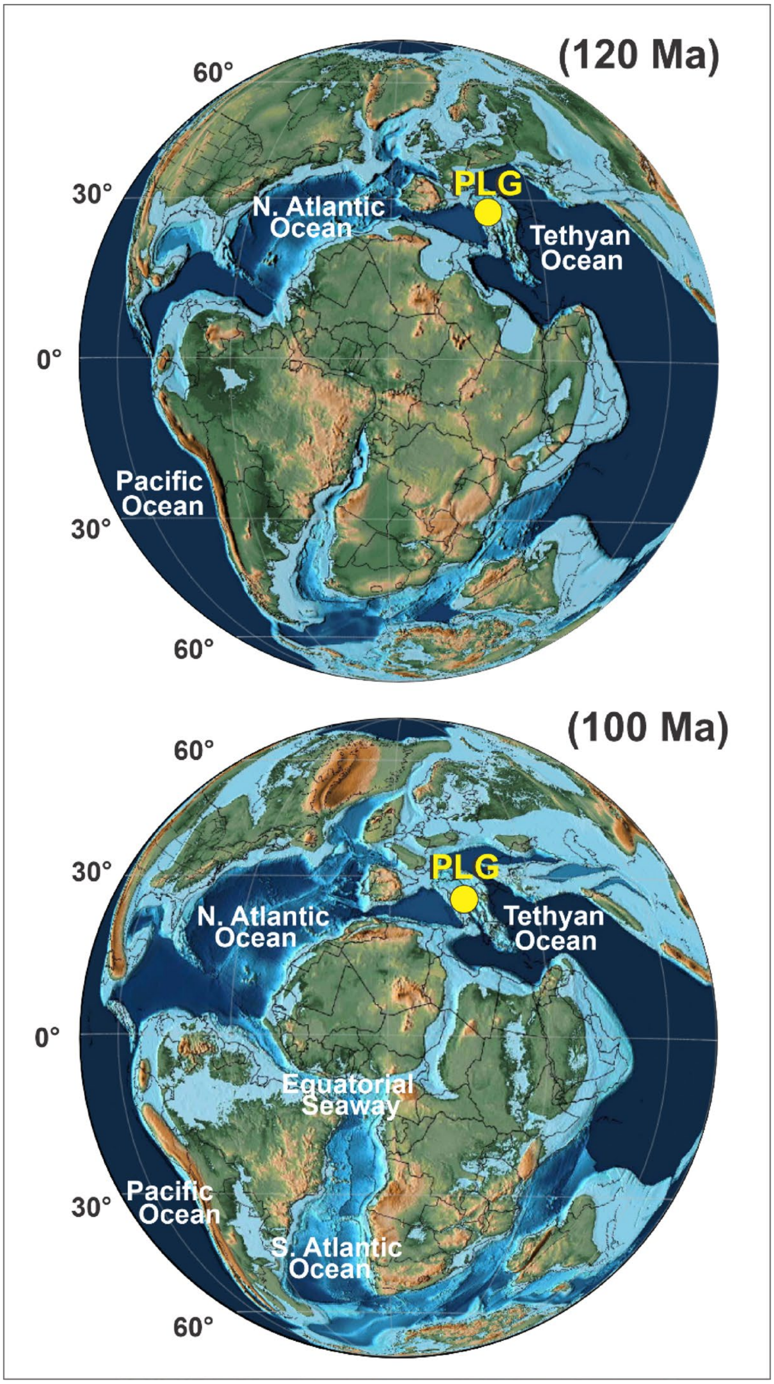

Fig. 1. Paleogeographic reconstructions at 120 and 100 Ma. Location of the PLG (yellow circle) core in the Tethyan realm (using Gplates 2.3.0).

Hayesites albiensis (NC8B), *Tranolithus orionatus* (NC8C); *Axopodorhabdus albianus* (NC9A), *Eiffellithus monechiae* (NC9B), and *Eiffellithus turriseiffelii* (NC10) in the Albian (Fig. 2).

Magnetic records and the Aptian–Albian astrochronology

MS measures the degree to which a sediment or rock is magnetized in the presence of a magnetic field, reflecting the concentration and grain size of magnetic minerals, such as magnetite. Low-field MS (χ, in m^3/kg) provides an indirect estimate of the abundance of paramagnetic and ferromagnetic minerals and has been widely applied in cyclostratigraphic studies[18]. Variations in MS can serve as proxies for changes in sediment supply, weathering intensity, or bioproductivity. ARM, which is sensitive to particle size, concentration, and mineralogy, similarly captures environmental and climatic variations through time by recording subtle shifts in sedimentation dynamics.

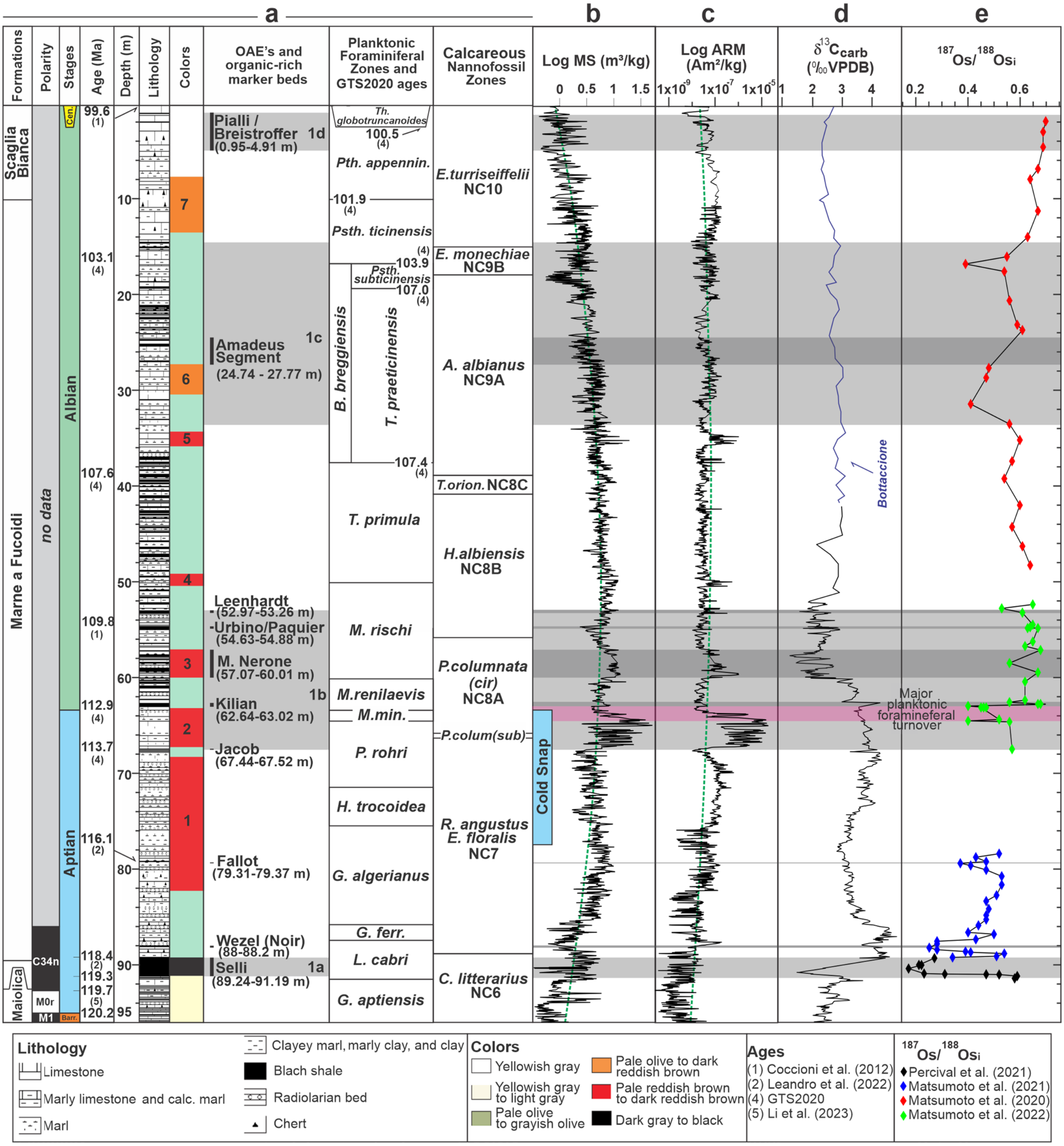

Fig. 2. Integrated stratigraphy of the studied interval in the PLG core. (**a**) The stratigraphic framework with formations, polarity, stages, age (Ma), lithology, sediment colors, OAEs, planktonic foraminiferal zones[1], and calcareous nannofossils zones of the PLG core[3,6,7,19,26,29,30]. OAEs are indicated by gray bands. Major planktonic foraminiferal turnover is highlighted in pale pink. Lithologies, color descriptions, and ages are given in the legend. (**b**) MS (black) with second-order polynomial trend (green-dashed line). (**c**) ARM (black) with second-order polynomial trend (green-dashed line). (**d**) δ^{13}C profile from the PLG core (black) and Bottaccione section (dark blue). (**e**) ^{187}Os/^{188}Os ratios[3,8,27,31]. *Bar.* = *Barremian, M.* = *Microhedbergella, min.* = *miniglobularis, P.* = *Paraticinella, H.* = *Hedbergella, G.* = *Globigerinelloides, ferr.* = *ferreolensis, L.* = *Leupoldina, B.* = *Biticinella, T.* = *Ticinella, Psth.* = *Pseudothalmanninella, Pth.* = *Parathalmanninella, Th.* = *Thalmanninella, C.* = *Chiastozygus, E.* = *Eprolithus, R.* = *Rhagodiscus, H.* = *Hayesites, T.* = *Tranolithus, A.* = *Axopodorhabdus, E.* = *Eiffellithus.*

In this study, log$_{10}$(MS) values range from − 0.48 to 1.71 m^3/kg (Fig. 2b), while log$_{10}$(ARM) values vary from 1×10^{-9} to 1×10^{-5} Am^2/kg (Fig. 2c). The highest MS and ARM values are observed in CORB 2, a lithofacies rich in clay, marl, and limestone in the Marne a Fucoidi Fm.[20], whereas the lowest values are found in the white lithofacies of the Maiolica Fm. Similar to CORB 2, CORBs 3, 4, and 5 exhibit elevated MS and ARM values (Fig. 2b,c).

Significant long- and short-wavelength quasiperiodic components are evident in both the MS and ARM datasets (Fig. 3). The 5π − MTM-Robust-AR(1) and eFFT spectra for both log$_{10}$(MS) and log$_{10}$(ARM) data (after detrending)—covering the stratigraphic interval from the top of the Albian (i.e., first occurrence (FO) *Th. globotruncanoides*[20]) to the base of the Aptian (i.e., M0r[26]) stages— distinguished three sets of low-frequency bands, common to both datasets and persistent throughout all studied intervals: (i) 1/1.75–1/2.63 m^{-1} (central frequency of ~ 1/2.3 m^{-1}); (ii) 1/0.52–1/0.66 m^{-1}; (iii) 1/0.17–1/0.30 m^{-1}); and (iv) 1/0.10–1/0.16 m^{-1}) (Figs. 3, 4 and Supplementary Figs. S1 and S2). The observed wavelength ratios verified for the log$_{10}$(MS) spectra (0.44,1.27,1.71,4.47,7.81,9.4 = 1.0,2.9,3.9,10.2,17.8,21.4) are compatible to those expected from the Milankovitch spectral peak ratios[37] for the top of the Aptian stage (~ 113 Ma): 1/405,1/125,1/95,1/38.7,1/22.9,1/18.4 = 1.0,3.2,4.3,10.5,17.7,22.0.

Furthermore, by applying the correlation coefficient (COCO)/evolutionary COCO (eCOCO) methods[38], optimal mean sedimentation rates of ~ 0.56 cm/kyr for MS data and ~ 0.61 cm/kyr for ARM data were determined, with more than six astronomical parameters each, and the null hypothesis (= no orbital forcing) significance levels were less than 0.0005 (Fig. 3e,l). These are consistent with mean sediment accumulation rates (SARs) of 0.561 cm/kyr (log$_{10}$(MS)) and 0.571 cm/kyr (log$_{10}$(ARM)) at null hypothesis significance levels < 0.001 obtained by application of the average spectral misfit (ASM) method[39,40] (Fig. 3g,o and Supplementary Figs. S1 and S2). Such findings allow us to infer that that MS and ARM datasets record orbitally-paced variations at (i) 405-kyr long eccentricity; (ii) 95–125-kyr short eccentricity; (iii) obliquity; and (iv) precession.

The phase analysis of the PLG core was previously conducted by Ramos et al.[22], which enables the estimation of the amplitude and phase of astronomical cycles during model fitting. We utilized their results prior to performing the astronomical tuning (see Ramos et al., 2024 for details). The phase of the 405-kyr sinusoidal component derived from the MS dataset is in phase with the long eccentricity signal (peak-to-peak, cave-to-cave). It is important to note that a phase offset between the classical La04 solution[41] and more recent orbital models[42–44] can introduce an age discrepancy of up to 185 kyr—specifically between La04 and ZB20a—when applied in astronomical tuning (see Supplementary Figures S4 and S5).

We then construct a ~ 405-kyr tuned age model for the MS data based on the g_2–g_5 target curve from the La2004 astronomical solution[38] and the 405-kyr long-eccentricity sinusoidal curve from a Gaussian bandpass filtering (0.02–0.35 cycles/m) applied to the log$_{10}$(MS) dataset, assuming as "tiepoints" the age of ~ 113.27 Ma (related to the Kilian Level[33,34]) and the M0r base (120.29 ± 0.09 Ma[32]) (Fig. 4a–d). The number of internal cycles within the Selli Level (OAE 1a) was estimated using the ages at the base (91.19 m; 119.534 Ma) and top (89.24 m; 118.273 Ma) of this event as proposed by Li et al.[16]. The anchored astrochronology, which covers the entire ~ 96.02 m PLG core, identifies 47 long-eccentricity cycles from the top of the Barremian (base of M0r Chron) through the top of the Albian stage (*E*17 to *E*33), implying a timespan of ~ 19.96 Myr (100.53–120.49 Ma). This new age model provides new ages for important geological events throughout the Aptian–Albian interval (Tables 1, 2): 1) ~ 6.97 Myr for the Aptian stage (GTS2020 = 8.2 Myr[1]) (from the base of Chron M0r and the LO of *M. renilaevis*), 2) ~ 12.82 Myr for the Albian (GTS2020 = 12.7 Myr) (from the LO of *M. renilaevis* to the LO of *Th. Globotruncanoides*), 3) ~ 430 kyr for the magnetic polarity Chron M0r; 4) 120.32 ± 0.203 Ma Ma for the Barremian–Aptian boundary and 5) the durations of the principal black shales and marker levels (e.g., the Amadeus Segment).

Astronomically dating Chron M0r, OAEs, organic-rich marker beds and CORBs

The chaotic behavior of the solar system[46,47] places a fundamental limit on the applicability of astronomical solutions for deep-time astrochronology. Even the most advanced models, such as ZB20x, are only reliable back to ~ 66 Ma[44], well short of the Aptian–Albian interval examined here. Consequently, the most robust anchor for early Cretaceous time calibration remains the stable 405-kyr eccentricity cycle, whose g_2–g_5 frequency term exhibits exceptional long-term stability[46]. We therefore employ the 405-kyr component from the La2004 solution, ensuring both methodological continuity with previous studies of the PLG core and practical equivalence with more recent orbital solutions.

Because no orbital solution is validated for the 100–120 Ma interval, age estimates must incorporate uncertainties arising from phase offsets among available models. Comparisons of the 405-kyr components from La2004[41], La2010a,b,c,d, and ZB20x show phase differences of up to ~ 185 kyr for 118–121 Ma, and the theoretical maximum offset between two fully anti-phased 405-kyr solutions is 202.5 kyr. We therefore assign a conservative uncertainty of ± 202.5 kyr to all astrochronologically derived ages. This uncertainty framework is supported by four high-precision absolute tie points for the base Aptian, in addition to well-established ages for the Kilian level and the top of the Albian, providing a robust structure for anchored astrochronology of the PLG core.

Although the filtered 405-kyr La2004 curve and the MS record exhibit an excellent phase match—differing by only ~ 100 kyr—such agreement may still be coincidental. The incorporation of a ± 202.5 kyr uncertainty therefore provides an appropriately cautious and defensible representation of age within the constraints of current astronomical solutions.

The presence of the M0r Chron in the PLG core reinforces its suitability as a candidate reference section for the Aptian and Albian stages[7,18,20,32]. This reverse chron is a proposed marker for the Barremian–Aptian boundary[1,48,49], and its age and duration are crucial factors for constraining past oceanic, tectonic, and geodynamic behavior[32]. Multiproxy orbital tuning for the PLG core provides an age of 120.32 ± 0.203 Ma for

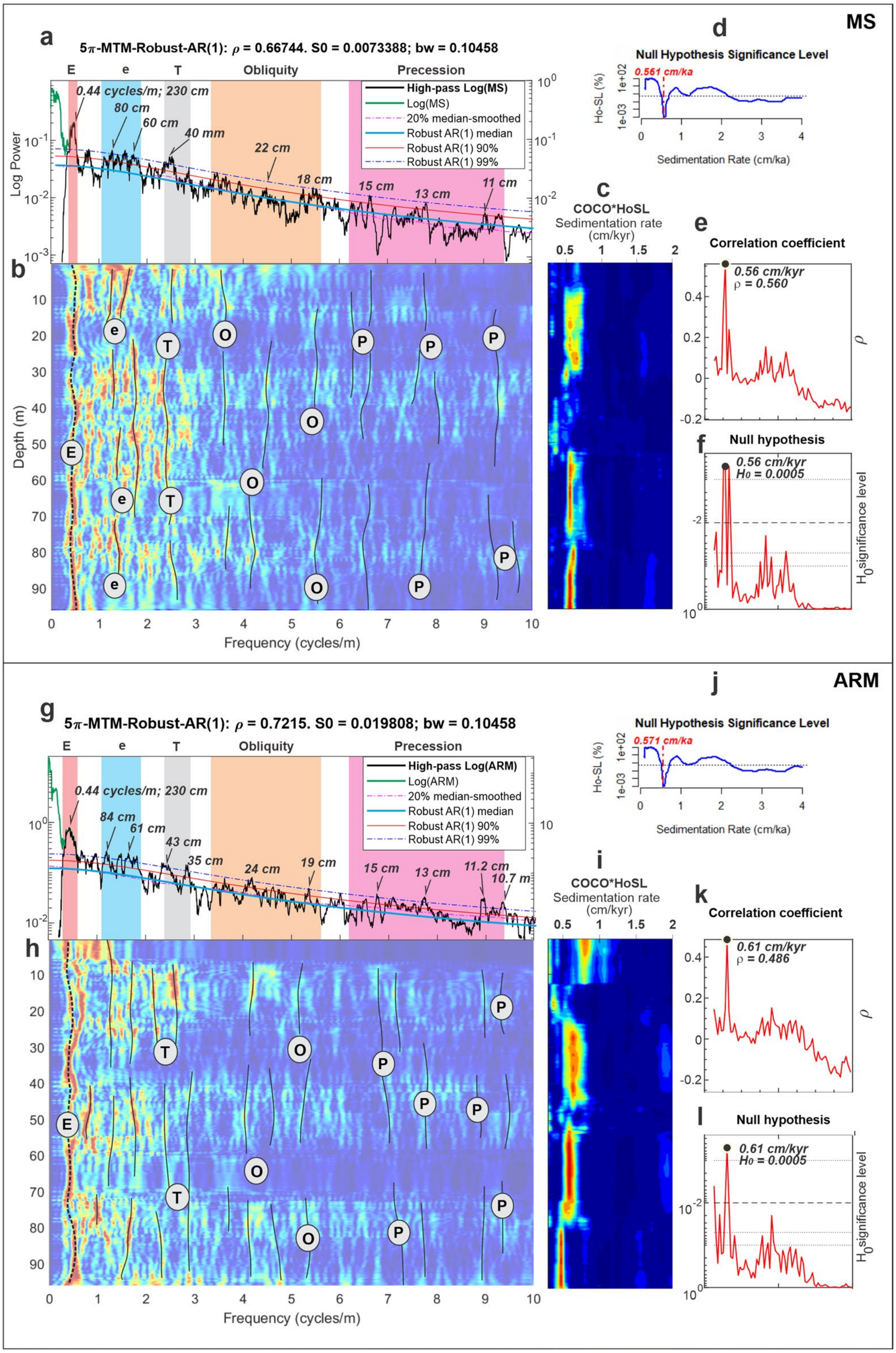

Fig. 3. Spectral analysis of the cyclostratigraphic series and SAR evaluation. (**a**–**f**) MS. (**g**–**l**) ARM. (**a**,**g**) Top: 5π multitaper power spectra, with the AR(1) red noise spectral model and median, 20% smoothed, 90%, and 99% confidence levels. Wavelengths of spectral peaks are labeled in cycles/m. MSB (green line) was removed by using high-pass filtering. (**b**,**h**) eFFT spectrograms, with each calculated spectrum normalized to 1. (**e**,**k**) Correlation coefficient (bulk) of COCO analysis[38], with the optimal values. (**c**,**i**) Evolutionary correlation coefficient plus null hypothesis map[38]. Details in Supplementary Figs. S1 and S2. (**f**,**l**) Null hypothesis testing of COCO analysis[38]. (**d**,**j**) Null hypothesis testing of ASM analysis[39,40] where the optimal value is highlighted in red. E = long eccentricity, e = short eccentricity, T = periodicities of ~ 60–70 kyr, O = obliquity, P = precession index.

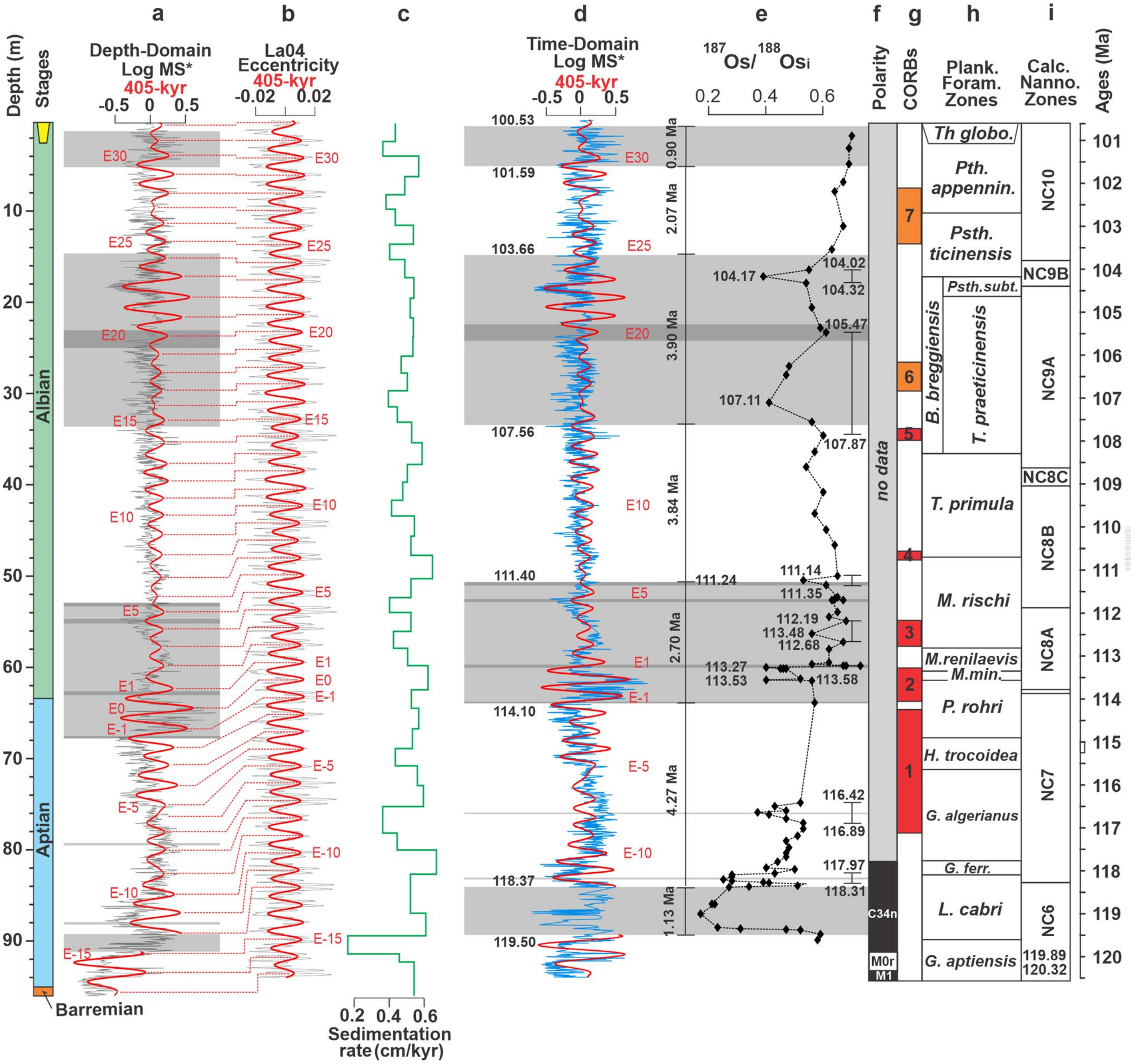

Fig. 4. Astronomical calibration of PLG. (**a**) Detrended log(MS), gray line, and 405-kyr component, red line. E-cycles[17] are numbered in red and correlated using a dashed red line. (**b**) La2004 orbital solution[45] (eccentricity only, gray line) and 405-kyr cycle (red) used for tuning. (**c**) SAR curve based on 405-kyr tuning (green line). (**d**) Tuned logarithmic scale MS data (blue line) with 405-kyr filter output (red line). (**e**) Tuned ^{187}Os/^{188}Os ratios[3,9,27,31]. The ages of the major unradiogenic shifts are highlighted. (**f**) PLG core magnetic polarity tuned[26]. Gray rectangles indicate no data. (**g**) Tuned PLG core CORBs[12] (Table 1). (**h**) Planktonic foraminifera zones[20,29] in the geological time domain (Table 2). (**i**) Calcareous nannofossil zones[20,29,30] in the geological time domain (Table 2). *M.* = *Microhedbergella, min.* = *miniglobularis, P.* = *Paraticinella, H.* = *Hedbergella, G.* = *Globigerinelloides, ferr.* = *ferreolensis, L.* = *Leupoldina, B.* = *Biticinella, T.* = *Ticinella, Psth.* = *Pseudothalmanninella, Pth.* = *Parathalmanninella, Th.* = *Thalmanninella.*

the base of Chron M0r (Barremian–Aptian boundary, Fig. 4, Table 1). This age is similar to the previously established ages (~ 120.2 Ma—by astrochronology[18]; 120.29 ± 0.09 Ma–by integration of U–Pb and ^{40}Ar/^{39}Ar ages[16,32]. For the top of Chron M0r, we obtain an age of 119.89 ± 0.203 Ma , ~ 200 kyr older than the central age, 119.70 ± 0.12 Ma[32]. Regardless of the astronomical solution used (La2004[41]; La2010x[42,43]; ZB20x[44]) (see Supplementary Figures S4 and S5), the astrochronology presented here indicates a timespan of approximately 430 kyr for the M0r Chron (based on the La2004 solution[41]), which is shorter than the 540 ± 37 kyr duration proposed by Li et al.[32].

Previous age estimates of the base of the Selli Level (OAE 1a) range from 124.55 to 119.30 Ma[18,50,51]. Our astrochronology indicates an age for the base of Selli Level of 119.50 ± 0.203 Ma and a timespan of 1.13 Myr. This value nearly coincides with the timespan proposed of 1.11 ± 0.11 Myr[51] (Table 1), and the U–Pb zircon ages of

	Depth (m)	Age (Ma)	Timespan (kyr)
Events and Chron			
OAE 1d	0.95–4.91	100.66–101.59	900
OAE 1c	14.50–33.57	103.66–107.56	3900
OAE 1b	52.09–67.52	111.40–114.10	2700
OAE 1a	89.24–91.19	118.37–119.50	1130
M0r Chron	92.70–95.10	119.89–120.32	430
Organic-rich marker			
Pialli Level	0.95–4.91	100.66–101.59	930
Amadeus Segment	22.77–24.77	105.29–105.66	370
Leenhardt Level	52.97–53.26	111.40–111.44	40
Urbino Level	54.63–54.88	111.67–111.71	40
Monte Nerone Level	57.07–60.01	112.17–112.77	600
Kilian Level	62.64–63.02	113.21–113.27	60
113/Jacob Level	67.44–67.52	114.08–114.10	20
Fallot Level	79.31–79.37	116.63–116.64	10
Wezel Level	88.00–88.20	118.17–118.21	40
Selli Level	89.24–91.19	118.37–119.50	1130
CORB #			
CORB 7	7.70–13.55	102.13–103.42	1290
CORB 6	27.30–30.43	106.18–106.84	660
CORB 5	34.40–35.89	107.72–107.99	270
CORB 4	49.18–50.46	110.56–110.77	210
CORB 3	57.07–60.01	112.17–112.77	600
CORB 2	63.02–67.28	113.28–114.05	770
CORB 1	68.31–82.24	114.25–117.11	2860

Table 1. Estimated timespans of OAEs, M0r Chron, organic-rich marker beds and CORBs. Depths for the upper and lower boundaries of the OAEs, organic-rich marker beds and CORBs identified in the PLG core[7,8,17] and the ages and timespans estimated in this work. All the ages presented in the table have a maximum age uncertainty of ± 0.203 kyr.

the tuffs constrain OAE 1a, indicating that it occurred between 118.273 ± 0.203 and 119.534 ± 0.203 Ma[16]. The correlation between the Selli event in the PLG core and the Cismon core using carbon ($\delta^{13}C$) stable isotope profiles and calcareous nannofossil zones[15,52] indicates that the brief hyperthermal event described at the onset of OAE 1a has an approximate duration of 90 kyr, suggesting that eccentricity orbital forcing may have acted as an amplifier of the climate-oceanographic disturbance caused by the 1.13 Myr volcanic long-term event that produced OAE 1a (Fig. 5 and Supplementary Fig. S3).

Despite the widespread acceptance of OEA 1b as a late Aptian–early Albian event[1,7], some controversies exist regarding OEA 1b divisions (or sub-events). Herrle et al.[53] have constrained OAE 1b in the Aptian–Albian boundary, an interval considerably restricted when compared to the definition by Coccioni et al.[7] and the GTS2020[1]. In this study, we set the base of the OAE 1b to the Jacob Level, and its top with the Leenhardt Level[8] where magnetic minerals have recorded significant environmental change. The base of OAE 1b has been estimated at 114.10 ± 0.203 Ma and the top at 111.40 ± 0.203 Ma, with an inferred timespan of 2.7 Myr. Our study reveals that the sub-events within OAE 1b, that are, the Jacob, Kilian, Monte Nerone, Urbino, and Leenhardt Levels, have central ages of 114.09, 113.25, 112.49, 111.69, and 111.42 ± 0.203 Ma, with durations of ~ 20, ~ 70, ~ 560, ~ 50, and ~ 380 kyr, respectively (Table 1).

Initially postulated as an anoxic event at the boundary between the Albian and Cenomanian (corresponding to OAE 1d[21]), OAE 1c is now defined as several layers moderately enriched in organic carbon in the *Biticinella breggiensis* planktonic foraminiferal zone[45]. OAE 1c has been interpreted as a detrital oceanic anoxic event characterized by high input of derived organic matter, resulting in the deposition of black shales. The Amadeus Segment[31,54], part of OAE 1c, though encompassing a long-term trend in NI[15], has a low nannofossil fertility index and high temperatures[36] (Fig. 5). Periodic anoxic conditions during the Amadeus segment were associated with warmer and less fertile surface waters, where variations in temperature or salinity (i.e., reduction of surface water density) are expected to be linked to Milankovitch cycles[36]. According to the results of this study, OAE 1c lasted 3.9 Myr (103.66–107.56 ± 0.203 Ma), within which the Amadeus segment is constrained at 105.66–105.29 ± 0.203 Ma.

Paleoenvironmental inferences across OAE 1d point to a warm climate (m-TI) and low fertility followed by a phase of lower temperature and higher fertility conditions within an overall warm climate that started prior to OAE 1d[15] (Fig. 5). Other UMB records exhibit a decrease in the NI prior to OAE 1d, followed by an increasing trend initiating in the middle of the Pialli Level. Except for a ~ 3.2 Myr interval, the Aptian is a period of generally low fertility (oligotrophy) compared to the Albian[15]. Between OAE 1b and OAE 1d, there is a long

	Depth (m)	Age (Ma)*	Timespan (kyr)
Planktonic foraminiferal zones			
*Th. globotruncanoides***	0.00	100.63	-
Pth. appenninica	10.00	102.70	2130
Psth. ticinensis	16.82	104.16	1460
Psth. subticinensis	19.35	104.64	500
T. praeticinensis	37.55	108.27	3630
T. primula	50.03	110.70	2430
M. rischi	60.20	112.80	2100
*M. renilaevis****	63.40	113.35	550
M. miniglobularis	64.50	113.56	210
P. rohri	71.47	114.91	1350
H. trocoidea	75.51	115.64	730
G. algerianus	85.76	117.77	2130
G. ferreolensis	87.44	118.08	310
L. cabri	91.35	119.60	1520
Calcareous nannofossil zones			
NC10A *(E. turriseiffelii)*	15.09	103.80	3270
NC9B *(E. monechiae)*	18.05	104.40	600
NC9A *(A. albianus)*	39.37	108.63	4230
NC8C *(T. orionatus)*	41.37	109.05	420
NC8B *(H. albiensis)*	55.79	111.88	2830
NC8A *(P. columnata (cir.))*	65.78	113.78	1900
NC8A *(P. columnata (sub.))*	66.34	113.88	100
NC7 *(E. floralis)*	88.67	118.28	4400

Table 2. Estimated timespans of biostratigraphic zones. Depths for the upper boundaries of the planktonic foraminiferal and the calcareous nannofossil zones identified in the PLG core[7,29,30] and this work, and the ages and timespans estimated in this work. All the ages presented in the table have a maximum age uncertainty of ± 0.203 kyr. (*) base of the biostratigraphic zone,(**) top of Albian,(***) top of Aptian.

phase (~ 8 Myr) of completely mesotrophic conditions, segmented by short periods of low fertility conditions. The maximum NI values were reached at the end of OAE 1d. There is no apparent relationship between the OAEs and fertility, as seen in the lower/middle Aptian, which exhibits long-term moderate nutrient conditions without any association with OAE (Fig. 5). Although OAE 1b is generally oligotrophic, black shale levels show high fertility[15].

The Pialli/Breistroffer Level in the UMB correlates with the lowermost part of the positive carbon isotopic excursion characterizing the late Albian–early Cenomanian OAE 1d. This interval is marked by frequent, well-marked, organic-rich layers and is called the Niveau Breistroffer[45]. For ~ 0.9 Myr (i.e., OAE 1d), anoxic conditions dominated in the Tethys Ocean. The black shale–poor facies deposited in the late Albian result from a shift in oceanic circulation from unstable to more stable conditions associated with a well-established thermocline and better-developed surface and bottom currents across interconnected basins[3]. Our study shows that, since the end of the deposition of the black shales related to OAE 1c (around ~ 103.7 Ma), the late Albian experienced a period of about 2.1 million years without significant deposition of black shale until the onset of OAE 1d at around ~ 101.6 Ma (Fig. 5).

CORBs and temperature during Aptian–Albian stages

CORBs are reddish to pinkish to brownish sedimentary rocks deposited in pelagic marine environments, comprising levels enriched in hematite and goethite[24,55,56]. In the PLG core, CORB deposition began at approximately 117.1 ± 0.203 Myr (or 82.24 m), 1.3 Myr after the occurrence of the organic beds of OAE 1a, where approximately 14 m of reddish lithologies were deposited. During this period, a significant paleoenvironmental change occurred, as shown by a break in ARM data (proxy for fine-grained magnetic minerals) and a sudden change in sediment color. The oxidizing environment that resulted in CORB 1[20] lasted approximately 2.86 Myr (Fig. 5, Table 1). A marked change in the input of magnetic minerals matches well with the onset of OAE 1b, where both MS and ARM indicate the highest input of fine magnetic material. This input corresponds to an interval without any fertility anomaly and is not associated with any abrupt temperature change[27]. Unlike the interval with high MS and ARM values present during the Monte Nerone Level, CORB 2 is unrelated to any significant $\delta^{13}C_{carb}$ shift.

Within OAE 1b, two oxidant events (CORBs 2 and 3) are notable for their high MS and ARM values. Unlike CORB 1, CORBs 2 and 3 have short durations (0.77 and 0.60 Myr, respectively). The modulation of the 405-kyr component in these intervals suggests that the orbital forcing acts as an amplifier, even though it is not the main cause of the oxidant character of the oceans. Detailed mineralogical studies have indicated that hematite,

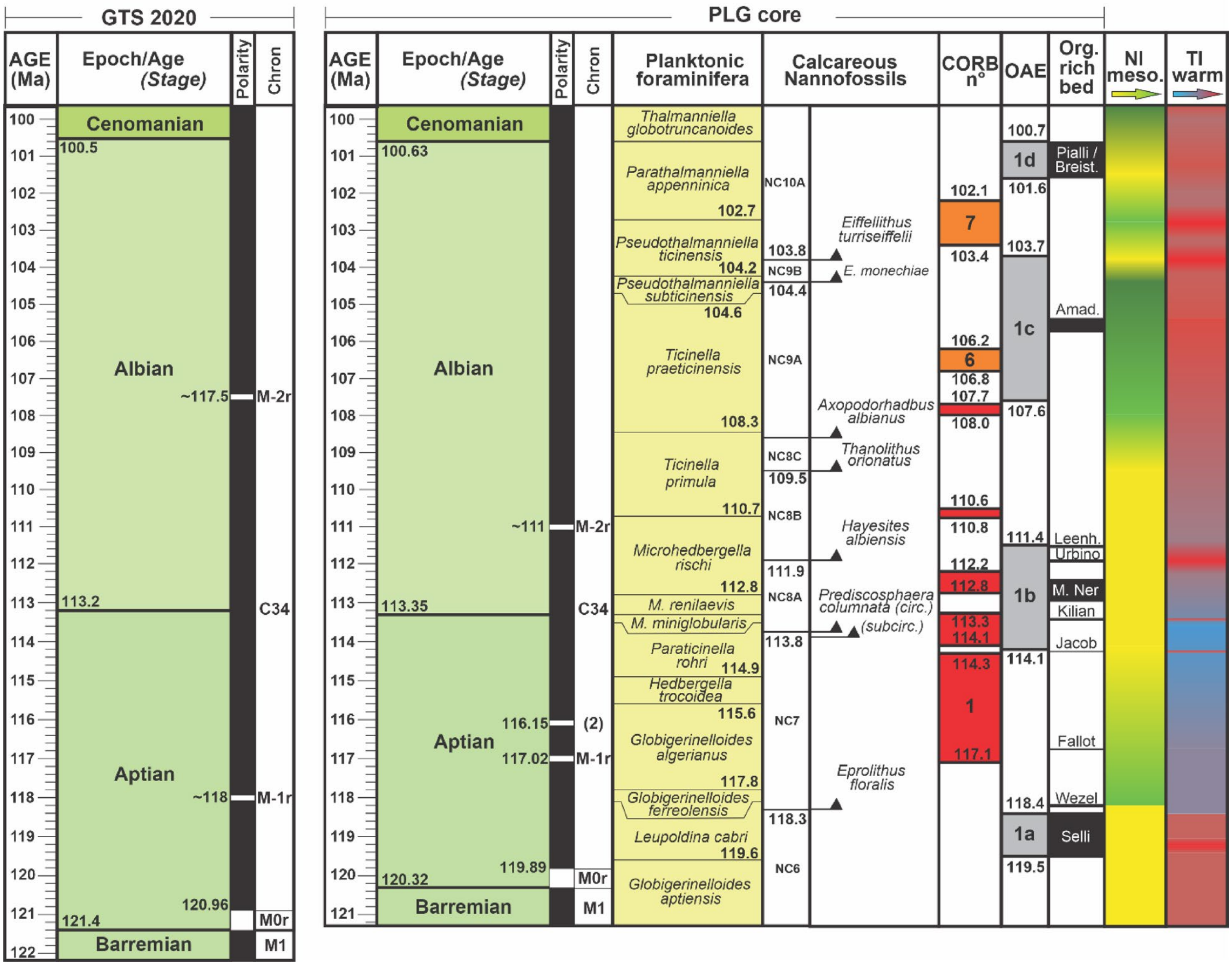

Fig. 5. New Aptian–Albian GTS. Modified Aptian–Albian timescale, including ages of the planktonic foraminifera zones and calcareous nannofossil zones. CORB and OAE ages are also presented. Organic-rich beds markers are indicated by black rectangles. (**h**) anchored astrochronology generated in this study and (**i**) corresponding E-cycles[17] in red. (**j**) arranged in the geological time domain. Extrapolated NI and TI indexes from Tethyan realm[15,36].

goethite, and Mn^{2+}-bearing calcite cause the red coloration of the CORBs in ODP 1049[55,56]. In the PLG core, the amount of hematite and goethite present in the red beds is likely controlled by short eccentricity and precession cycles, which are modulated by long eccentricity. Long-term cycles (~ 1.2 and ~ 2.4 Myr) are described in Cretaceous geological records[46,47,57,58]. Based on this timespan, we suggest that the large modulation cycle of obliquity, ~ 1 Myr (or a resonant state of the ~ 2 Myr eccentricity cycle[47,57]), may control the differential input of fine magnetic minerals[57].

After the end of OAE 1c and before the major paleogeographic and palaeoceanographic changes at the end of the Albian, a new predominant oxidant period lasting 1.29 Myr begins (Table 1). Similar to CORB 6, CORB 7 is locally represented by predominantly orange-colored sediments and does not exhibit high values of MS and ARM. This interval preceding OAE 1d is characterized by a mesotrophic nutrient level and marks the period with the highest temperatures throughout the Albian. The end of CORB 7 represents a significant environmental change glimpsed through (i) the onset of the positive excursion of $\delta^{13}C_{carb}$ and, consequently, the beginning of OAE 1d; (ii) the return to oligotrophic conditions; (iii) a new warming period, recorded by the positive excursion of $\delta^{18}O_{carb}$ and m-TI SSTs (°C); and (iv) the deposition of the rare black shales of the Pialli Level[9,15,29].

Through the analysis of carbon isotope curves and calcareous nannofossil zones, we have correlated the measurements of the NI and TI from various sections and classic cores within the Tethyan context (i.e., Cismon core, Piobbico, and Mt. Petrano)[15,36] with the PLG core, allowing for precise positioning within the geological time scale (Fig. 5 and Supplementary Fig. S3). In general, the m-TI data indicate that the Albian was warmer than the Aptian[15,36]. The m-TI suggests that temperatures remained consistently high until the end of OAE 1a, enduring for approximately 2.1 million years, with a rapid warming event occurring at the onset of OAE 1a. After OAE 1a, the m-TI data show a cooling trend that persisted through the late Aptian (~ 5 million years). Notably, no clear correlation emerges between temperatures and the OAEs. Despite a pronounced temperature drop immediately following OAE 1a, gradual warming occurred during OAE 1b, with thermal maxima associated with black shale deposition. A long-term pattern of elevated temperatures extends beyond OAE 1c, while temperature reductions are observed within OAE 1d.

In the Tethyan Ocean, the lower portion of the *H. trocoidea* planktonic foraminiferal zone marks the cold snap[18,23], a mid-Cretaceous global cooling event characterized by the breakdown of warm, equable climate conditions[23,58,59]. Our study, based on correlations between the PLG core and Tethyan sections[15,18,23,36] (Supplementary Fig. S3), suggests that mild temperatures prevailed during most of the Aptian (~ 118.4 to 113.4 Ma). This "cold" period, characterized by the lowest surface water temperatures (as indicated by TI[15]), corresponds with elevated $\delta^{13}C$ values, suggesting changes in oceanic circulation, carbon sequestration at the surface, and potential incorporation of carbon into marine organisms. Despite the lowest temperatures occurring within the cold snap interval[16,18], the interval may be extended to between 113.4 and 118.4 Ma, based on temperature data[15] and the inferred paleoclimatic stability that allowed for the continuous deposition of CORB 1 over this time span (Fig. 5). Evidence of a milder climate spans from the NC6 nannofossil zone to the lower/middle NC8 zone[15,30] corresponding to the deposition of CORBs 1 and 2[20], with the coldest temperatures (~ 115.5 to 113.4 Ma) confined to the upper Aptian. The paleoenvironmental shift likely began earlier (*G. algerianus zone*, ~ 118.4 Ma), marked by sharp changes in $\delta^{18}O$ values and TI[15], as reflected by a sudden shift in sediment color[18,20].

The most pronounced break in the maximum magnitudes of short-term sea-level variation (at the end of Trend II[14]) is associated with the termination of the Aptian cold snap. During this transition, the dominant high-frequency, high-amplitude, orbitally forced glacio-eustasy that characterized the late Aptian was replaced by aquifer-eustasy. Consequently, the elevated magnitude values observed during the Aptian gave way to significantly lower values in the Albian[14]. This shift coincides with the final rupture of Gondwana and the establishment of full marine connectivity between the South and North Atlantic Oceans[13] suggesting that tectonic reorganization played a key role in altering eustatic drivers.

Over intermediate timescales of 2–10 Myr, dynamic topography exerts a significant influence on sea-level change and cannot be disregarded. Notably, the late Aptian increase in Fe and Ti concentrations—proxies for enhanced weathering and aquifer discharge—indicates that during the Albian, aquifer-eustasy modest eustatic fluctuations may have overtaken astronomically driven climate mechanisms as the primary control on global sea-level variations[22].

Aptian–Albian bioevents

The bioevents of the PLG core provide a detailed biostratigraphic scheme based on planktonic foraminifera and calcareous nannofossils[7,20,29,30]. Our study also provides new ages for planktonic foraminiferal and calcareous nannofossil bioevents (Fig. 4 and Table 2). Through this study, using as reference the PLG core osmium peaks and carbon and oxygen isotope excursions (all of them with supra-regional to global character), it is possible to refine the biozonations and assess the degree of diachroneity[59] and the patterns of species dispersal between the Tethyan Ocean and other oceanic regions.

The ages and durations of the bioevents in the PLG core (Table 2) indicate that the top of the Aptian and Albian have ages of 113.35 ± 0.203 (LO of *M. renilaevis*) and 100.63 ± 0.203 Ma (LO of *Th. globotruncanoides*), respectively. These values are very close to the ages proposed in the GTS2020[1]. However, our astrochronology enables refinement of the ages within these stages, and there are large discrepancies between the ages obtained in our work and those in the GTS2020. For example, the LO of *Ticinella praeticinensis* occurs 0.87 Myr earlier in our astrochronology than the GTS2020 (108.27 ± 0.203 Ma in the PLG and 107.4 Ma in the GTS2020). The top of this biozone occurs at 104.64 ± 0.203 Ma in the PLG and 107.0 Ma in the GTS2020, resulting in a difference of 2.76 Myr. In other words, the *T. praeticinensis* planktonic foraminiferal zone lasts 0.4 Myr in the GTS2020 age model and 3.63 Myr in our age model.

The *Leupoldina cabri* planktonic foraminiferal zone, correlated in the PLG core with the unradiogenic shifts associated with the Selli and Wezel Levels, has its base at 119.60 ± 0.203 Ma and spans 1.52 Myr. The *Globigerinelloides algerianus* planktonic foraminiferal zone (117.77–115.64 ± 0.203 Ma), associated with the ISEA reverse chron (M"-1r")[60], has an important $^{187}Os/^{188}Os_i$ peak in its intermediate portion. These two events could potentially serve as tiepoints for correlations between basins. The short time interval of the *Microhedbergella miniglobularis* zone (timespan of 0.21 Myr) and the base of the *M. renilaevis* zone (113.35 ± 0.203 Ma) is well-anchored by two $^{187}Os/^{188}Os_i$ peaks, serving as an excellent marker for the top of the Aptian[2]. The sub-events of the OAE 1b Monte Nerone and Urbino/Paquier Levels are included in the *Microhedbergella rischi* zone (110.70–112.80 ± 0.203 Ma)[7,20].

Assuming that the latter has a global character, the diachroneity between the species of this zone can be evaluated in cyclostratigraphic studies using this black shale level as a tiepoint. Despite the long-lasting period related to the *T. praeticinensis* (104.64–108.27 ± 0.203 Ma) and *B. breggiensis* (104.16–108.27 ± 0.203 Ma) zones, significant internal markers within these zones can be used as temporal anchors. In addition to CORB 5 (107.56–107.99 ± 0.203 Ma, basal portion of these zones) and CORB 6 (106.18–106.84 ± 0.203 Ma), the peak of $^{187}Os/^{188}Os_i$ (107.11 Ma) between these two CORBs can serve as an excellent temporal marker to evaluate both the diachroneity of species and issues involving the local vs. global nature of the CORBs[24,55,56]. Furthermore, the second $^{187}Os/^{188}Os_i$ peak (104.17 Ma) is practically coincident with the LO of *B. breggiensis*.

The boundary between the NC6 and NC7 *Eprolithus floralis* calcareous nannofossil zones[30] occurs at 118.28 Ma, between the Selli and Wezel events. This boundary is also marked by high $^{187}Os/^{188}Os_i$. The top of the NC7 zone (113.88 ± 0.203 Ma, Table 2), which marks the base of the NC8A zone (*P. columnata*[30]), is located at the PLG core near the base of OAE 1b[22]. High values of MS and ARM (reflecting modulation in the *anchored astrochronology* obtained) coincide with this boundary, highlighting it as an important marker for future correlations between basins. The boundary between the NC8A and NC8B (*H. albiensis*[30]) zones, still within the context of OAE 1b, is stratigraphically placed just below the Urbino/Paquier Level[7,20,22] in an interval characterized by the absence of unradiogenic Os shifts[8,61]. The NC8C zone (*T. orionatus*, 108.63 to 109.05 Ma) is set in the upper part of the *T. primula* zone, near the boundary with *T. praeticinensis*. In the lower part of the NC9A zone (*A. albianus*[30], 104.40 to 108.63 ± 0.203 Ma), a significant unradiogenic $^{187}Os/^{188}Os_i$ shift occurs at 107.11 Ma. The NC9B zone (*E. monechiae*[30]) can be associated with OAE 1c. Within the context of OAE 1c, a second unradiogenic Os shift (104.17 Ma, Fig. 4e) marks the transition between the NC9A and NC9B zones. Starting at 103.80 ± 0.203 Ma (Table 2), the NC10 zone (*E. turriseiffelii*[30]) begins and is characterized by the absence of unradiogenic $^{187}Os/^{188}Os_i$ shifts and the presence of OAE 1d in its uppermost portion.

Ages, timespans, and consequences of unradiogenic shifts

The most significant unradiogenic shift begins at 119.48 ± 0.203 Ma and spans the entire OAE 1a interval (Fig. 2). A second shift, lasting 0.34 Myr (118.31–118.97 ± 0.203 Ma), is longer than the Wezel event (0.04 Myr). The third unradiogenic shift, associated with the Fallot Level, occurs between 116.89 and 116.42 ± 0.203 Ma. Similar to the second shift, this shift lasts longer than the deposition of the black shale (0.47 Ma vs. 0.01 Ma; Table 1).

OAE 1b, a mix of volcanic and monsoon-driven OAEs[8], was triggered by atmospheric circulation reorganization[45]. This event is linked to Hg anomalies[19], suggesting volcanism during this period. The first shift of OAE 1b (113.56 ± 0.203 Ma) coincides with a major planktonic foraminiferal turnover[7,56,62], lasting ~ 0.02 Myr and showing a peak in Hg/TOC, reinforcing the link between volcanic activity and ocean acidification[3]. Additionally, the Kilian, Monte Nerone (central interval), and Leenhardt subevents are tied to unradiogenic shifts and Hg anomalies[19].

OAE 1c features two unradiogenic shifts. The first, beginning at 107.87 Ma with a peak at 107.11 Ma and pre-shift values at 105.47 Ma, is linked to the onset of the anoxic event. The Amadeus Segment lacks Os data, preventing determination of any unradiogenic shifts. A second shift starts at 104.32 Ma, peaking at 104.17 Ma (*Pseudothalmanninella subticinensis* planktonic foraminiferal zone). Though within OAE 1c, no black shale is associated with this shift. The monsoon-driven nature of OAE 1d[8] is evident at the top of the studied interval, where the anoxic event lacks any Os shift.

The 405-kyr long-eccentricity cycles derived from MS and ARM data (0.44 cycles/cm or 2.3 m) provide high-resolution cyclostratigraphy. Using astronomical tuning of the long-eccentricity low-pass filter from the La2004 orbital solution[41], we: (i) propose a anchored astrochronology based on 49 long-eccentricity cycles, enabling a ~ 20 Myr age model from the top of the Barremian to the top of the Albian; (ii) refine the timing and duration of OAEs, black shales, CORBs, and Os unradiogenic shifts; and (iii) estimate bioevent durations using our age model for the PLG core. This study establishes a new chronostratigraphic framework for the Aptian–Albian, enhancing understanding of the biological, chemical, and geomagnetic events and updating the current GTS.

Age model for Aptian–Albian events

The Aptian-Albian interval is characterized by abrupt paleoclimatic shifts, driven by extensive volcanic activity[3,8,17,63] and orbital forcings that intensified the monsoonal system[22,31]. Some OAEs and black shales are linked to peaks in volcanism, while others display mixed features, including OAEs and organic-rich layers associated with monsoonal activity[8,22]. Our study places key events within the geological timescale, offering a clearer cause-and-effect relationship (Fig. 6).

The longest volcanic period (1.13 Myr) in the Aptian-Albian begins with a brief thermal maximum19. The nannoconid crisis[18], occurring ~ 100 kyr before OAE 1a, is likely tied to volcanism starting at 119.50 ± 0.203 Ma. The delay between these events may reflect Os residence time (~ 50 kyr[18]) and the environmental response to early volcanic activity. This volcanic phase persists until ~ 118 Ma, when the Aptian icehouse interlude[15,18,23,53,57]. A subsequent volcanism peak (116.89 to 116.42 Ma) leads to the deposition of Fallot black shale. This mild climate period, with possible ice at high latitudes, shows a long-term carbon curve shift. Two hyperthermals occur at the end of the period: the first, linked to Jacob/113 black shales with no volcanism; the second, related to a unradiogenic $^{187}Os/^{188}Osi$ shift and volcanism[8,22]. This volcanism peak marks a significant carbon isotope shift, ends glendonites and dropstones, and concludes the Aptian icehouse interlude.

Foraminiferal turnover[62] suggests the greenhouse shift was a major change in the ocean–atmosphere system. In OAE 1b, a new hyperthermal causes a significant carbon curve shift and deposition of the Urbino Level. The lack of a unradiogenic $^{187}Os/^{188}Os_i$ anomaly and paleoclimatic proxies link this shale to a monsoonal event[22]. OAE 1b ends with a volcanic event leading to the Leenhardt Level (Fig. 6). Sporadic volcanism, driven by orbital forcings and high fertility, deposits black shales during OAE 1c. The Amadeus Segment, the main level, lacks a unradiogenic $^{187}Os/^{188}Osi$ shift and may relate to orbital monsoonal activity[31]. OAE 1d, characterized by no volcanic activity, is marked as an oligotrophic period[15].

The correlation between unradiogenic osmium shifts, volcanism, and climate perturbations strengthens the link between astronomical forcing, paleogeographic evolution, and oceanic redox fluctuations during the Aptian-Albian. The updated chronostratigraphic model refines the existing GTS, providing a foundation for inter-basin correlations and enhancing our understanding of the complex interactions between tectonic, climatic, and biotic processes in the Early Cretaceous.

Materials and methods

Geological setting and sampling strategy

The PLG core (lat. 43°32′42.72"N; long. 12°32′40.92"E) was recovered at Poggio le Guaine (northern Apennines, central Italy), a site known to contain one of the most continuous, comprehensive, and well-preserved Aptian–Albian sedimentary sequence. The PLG drill hole cored the uppermost Barremian–lowermost Cenomanian succession of the Umbria-Marche Basin, deposited in the southern margin of the central-western Tethys Ocean[7,20]. These pelagic sediments formed following the lithification of the nannofossil-planktonic foraminiferal ooze deposited well above the calcite compensation depth at middle to lower bathyal depths (1000–1500 m)

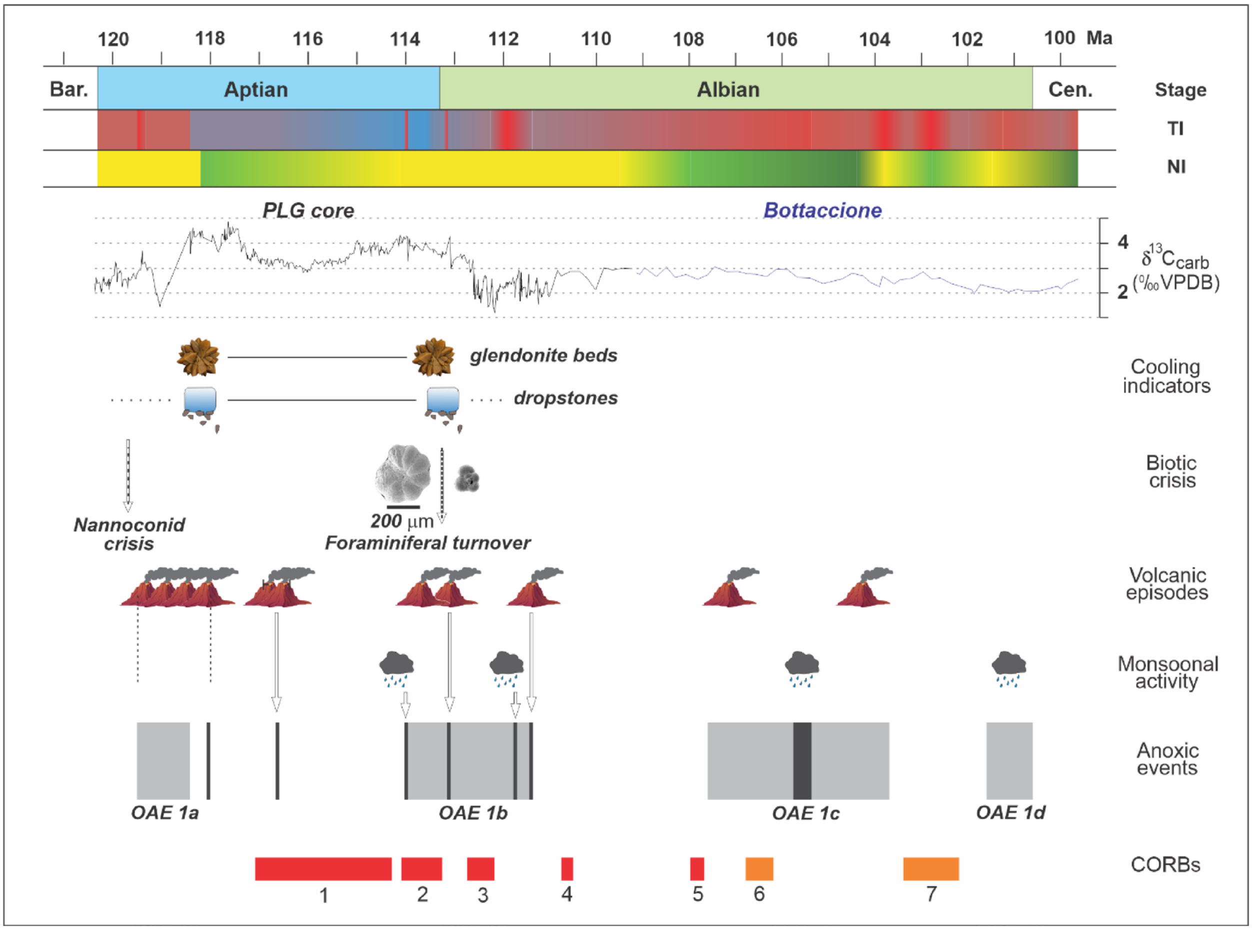

Fig. 6. Aptian–Albian events. Aptian–Albian events, including sedimentological indications of the Aptian icehouse interlude, biotic crisis, volcanic episodes and monsoonal activity, responsible for the implantation of the OAEs and the deposition of the black shale levels.

and ~ 20°N paleolatitude[7,18,20] and provides an uninterrupted archive of fossil-rich pelagic strata from 100.5 to 121.4 Ma.

The uppermost Barremian–lowermost Cenomanian succession investigated here is represented by the thin-medium white to gray limestones interbedded with the black shales of the Maiolica Formation and by the overlying distinctive varicolored interlude with more shale of the lower part of the Marne a Fucoidi Formation. The latter consists of thinly interbedded pale reddish to dark reddish, pale olive to dark reddish-brown, and pale olive to grayish olive marlstones and calcareous marlstones together with dark gray to black carbon-rich shales, commonly with a low carbonate content, and yellowish-gray to light gray more or less argillaceous limestones.

Some distinctive organic-rich black shale and calcareous mudstone marker beds occur within the Aptian interval, some of which have been correlated with black shale horizons elsewhere with varying degrees of success and identified as the regional sedimentary expression from the OAE 1a and OAE 1d[7,8,18,20,26]. From bottom to top, they are: 1) the Selli Level, known as the organic-rich expression of OAE 1a; 2) the Wezel Level horizon; 3) the Fallot Level; 4) the 113/Jacob Level; 5) the Kilian Level; 6) the Monte Nerone black shales cluster Level; 7) the Urbino/Paquier Level; 8) the Leenhardt Level; 9) the Amadeus segment black shale cluster Level and; 10) the Pialli/Breistroffer black shale cluster Level.

Discrete ~ 8 cm^3 cubic samples were then retrieved from the center of the split working halves for paleomagnetic analysis. A total of 3,092 cubic samples were collected along the studied portion of the PLG core (from 96.02 to 0.36 m; average sampling resolution of ~ 3 cm). A total of 355 paleomagnetic cubic samples were also used to measure the stable isotopes ($\delta^{13}C$) with a ~ 10-cm resolution.

Rock magnetism

Rock magnetic parameters have largely been used to identify orbital cycles in sedimentary strata[54] because they are fast, low-cost, and non-destructive. In addition, they allow analysing large sample populations. Rock magnetic measurements indicate that magnetite serves as the primary magnetic carrier[26]. Low-field MS (χ, in m^3/kg) is an indirect measurement of the concentration of paramagnetic and ferromagnetic minerals in geological samples. It has been extensively used as a proxy for terrestrial detrital input in mixed carbonate–clay successions[46]. Nevertheless, variations in the MS occur due to several other factors, such as magnetic mineral concentration, composition, grain size, and shape[57].

The ARM has been considered in cyclostratigraphy investigations as an alternative proxy to MS[57]. Notably, the ARM obtained at 100 mT (hereafter referred to as ARM) is useful in providing information on fine-grained (< 20 µm) low-coercivity ferromagnetic minerals[57]. Our rock magnetic cyclostratigraphy analyses comprise both MS and ARM datasets to better assess and compare the spectral content and depositional time range. The MS measurements were performed at the Laboratório de Paleomagnetismo of Universidade de São Paulo (USPMag). They were made on an MFK1-FA Multi-Function Kappabridge at an operating frequency of 976 Hz in a field of 200 A/m. The acquisition of the ARM dataset was performed by the following protocol: remanence measurements were all made in a SQUID magnetometer, model 755 (2G-Enterprises), housed in a magnetically shielded room with internal field < 500 nT at USPMag. The samples underwent a stepwise alternating field (AF) demagnetization over 17 steps: 0–4 mT (step = 2 mT), 4–10 mT (step = 3 mT), 10–40 mT (step = 5 mT), 40–100 mT (step = 10 mT). After AF demagnetization, the sample was submitted to a stepwise ARM acquisition along the same AF demagnetization steps until 100 mT with a direct current bias field of 0.05 mT.

Planktonic foraminifera and calcareous nannofossils

The sample set consists of bulk rocks. At least 30 g of rock were processed for each sample using different methodologies according to the lithology and hardness of the sediment. Samples from softer lithologies were soaked in hydrogen peroxide and desogen. Where required, samples were additionally treated with the surfactant benzalkonium chloride. Samples from hard lithologies were mechanically disaggregated into small fragments (3–8 mm) and treated using the cold acetolysis technique by sieving through a 40-µm mesh and drying at 50 °C. The cold acetolysis method enabled the extraction of easily identifiable foraminifera, even from indurated limestones. This technique offered the possibility of accurate taxonomic determination and detailed analyses of planktonic foraminiferal assemblages, allowing more precise placement of primary and secondary bioevents and zonal boundaries.

Planktonic foraminifera from the washed residues were studied under a stereomicroscope to characterize assemblages and identify biostratigraphic marker species. Taxonomic concepts for genera and species of reference studies were followed (refs.[7,53,62]). Calcareous nannofossil assemblages were semi-quantitatively investigated using a Zeiss AxioCam imaging polarizing light microscope at 1250 × magnification. The sediment was processed to obtain homogeneous smear slides following the standard preparation technique: a small rock chip was powdered in a mortar with distilled water buffered with ammonium. A few drops of the solution were smeared on a cover glass, dried on a hot plate, and mounted on a glass slide with two drops of Norland optical adhesive. A total of 45 smear slides were analyzed; in each slide, nannofossil species abundances were logged as follows: A = abundant, > 1 specimen/field of view. C = Common, 1 specimen in 50/fields of view. F = Few, 1 specimen in 100/fields of view. R = Rare, 1 specimen in 200/fields of view. For this analysis, 300 fields of view were scanned on each slide. Calcareous nannofossil zones are updated from Lamm et al.[30] and Coccioni and Frontalini[29].

Cyclostratigraphy

Cyclostratigraphic analyses for MS and ARM datasets were conducted with Acycle (version 2.4.1[64]) and Astrochron (version 1.2[39,40]). All MS and ARM datasets were log-transformed to harmonize fluctuations[65] before the resampling process every 2 cm. After interpolation, the datasets were detrended using a second-order polynomial curve. Spectral analysis was conducted using the prolate multitaper spectral estimator, comparing it against a robust red noise null model, with confidence levels set at the mean, 90%, 95%, 99%, and 99.9%. The MS and ARM series carry a long-term trend (Million-year scale band[18]) with high amplitude, leading to power leakage from the low-frequency components into the 405-kyr cycle; therefore, both series were high-passed (cutoff of 0.02 cycles/m). In the SAR analysis, MSB signals were removed to suppress the very high amplitude for the low frequencies.

Gaussian bandpass filters (0.02 and 0.35 cycles/m) were applied to isolate the interpreted long-eccentricity component sinusoidal curve from the datasets tuned prior to the tuning process according to the g_2–g_5 target curve from the La2004 astronomical solution[41]. Additionally, we performed evolutionary Fast Fourier Transform (eFFT) analyses[57] to observe the continuity of the spectral frequencies along the MS and ARM series. The sediment accumulation rates were evaluated throughout the PLG using COCO/eCOCO[38] and ASM[39,40]. We conducted the COCO/eCOCO analysis by using 2,000 Monte Carlo simulations, applying sedimentation rates ranging from 0.26 to 10 cm/kyr referenced to the La2004 solution with a median age of 115 Ma (maximum frequency of 0.06/kyr), employing the Pearson correlation method.

Additionally, we utilized the time–frequency implementation of the ASM from the Astrochron package, which allows for quantitative testing of the orbital influence on sedimentation. We used the vector of the candidate astronomical cycles observed in the MS data spectrum (0.44, 1.27, 1.71, 4.47, 7.81, 9.4), the vector of the theoretical astronomical frequencies (1/405, 1/125, 1/95, 1/38.7, 1/22.9, 1/18.4), a Nyquist frequency of 25 cycles/m, and sedimentation rates ranging from 0.26 to 4.0 cm/ka (100 sedimentation rates). We conducted 100,000 Monte Carlo simulations for significance testing. These results enabled us to reject the null hypothesis that the observed spectrum was derived from a random signal with a high degree of confidence.

Data availability

The MS and ARM datasets used in this study are available in the Zenodo repository https:doi.org/https://doi.org/10.5281/zenodo.6383426 .

Code availability

All mathematical treatments were performed with the freeware Acycle designed by ref.[64] and Astrochron R Package ref.[39,40].

Received: 6 May 2025; Accepted: 7 January 2026

References

1. Gale, A. S., Mutterlose, J. & Batenburg, S. In *Geologic Time Scale 2020*, (eds. Gradstein, F. M., Ogg, J. G., Schmitz, M. D., Ogg, G. M.) 1023–1068.
2. Judd, E. J. et al. A 485-million-year history of Earth's surface temperature. *Science* **385**(1316), 1–9 (2024).
3. Wignall, P. B. Large igneous provinces and mass extinctions. *Earth Sci. Rev.* **53**, 1–33 (2001).
4. *Large igneous province record through time and implications for secular environmental changes and geological time-scale boundaries*. Ernst, R.E., Bond, D.P. et al. From: Ernst, R.E., Dickson, A.J. and Bekker, A. (eds) Large Igneous Provinces: a Driver of Global Environmental and Biotic Changes. AGU, *Geophysical Monographs* **255**: 3–26 (2021).
5. *Radiometric constraints on the timing, tempo, and effects of large igneous province emplacement*. Kasbohm, J., Schoene, B. and Burgess, S. From: Ernst, R.E., Dickson, A.J. and Bekker, A. (eds) Large Igneous Provinces: A Driver of Global Environmental and Biotic Changes. AGU, *Geophysical Monographs* **255**: 27–82 (2021).
6. Jiang, Q., Jourdan, F., Olierook, H. K. & Merle, R. E. An appraisal of the ages of Phanerozoic large igneous provinces. *Earth Sci. Rev.* **237**, 104314 (2023).
7. Coccioni, R. et al. The neglected history of Oceanic Anoxic Event 1b: insights and new data from the Poggio le Guaine section (Umbria–Marche Basin). *Stratigraphy* **11**, 245–282 (2014).
8. Matsumoto, H. et al. Mid-Cretaceous marine Os isotope evidence for heterogeneous cause of oceanic anoxic events. *Nat. Commun.* **13**, 239 (2022).
9. Giorgioni, M. et al. Paleoceanographic changes during the Albian-Cenomanian in the Tethys and North Atlantic and the onset of the Cretaceous chalk. *Glob. Planet. Change* **126**, 46–61 (2015).
10. Schlanger, S. O. & Jenkyns, H. C. Cretaceous oceanic anoxic events: causes and consequences. *Geol. en. Mijnb.* **55**, 179–184 (1976).
11. Simmons, M. D., et al. Phanerozoic eustasy. In *Geologic Time Scale 2020*, (eds. Gradstein, F. M., Ogg, J. G., Schmitz, M. D., Ogg, G. M.) 357–387 (2020).
12. Conrad, C. P. The solid Earth's influence on sea-level. *Geol. Soc. Am. Bull.* **125**(7–8), 1027–1052. https://doi.org/10.1130/B30764.1 (2013).
13. Dummann, W., et al. The impact of Early Cretaceous gateway evolution on ocean circulation and organic carbon burial in the emerging South Atlantic and Southern Ocean basins. *Earth Planet. Sci. Lett.* **530**, 115890. https://doi.org/10.1016/j.epsl.2019.115890 (2020).
14. Ray, D. C., et al. The magnitude and cause of short-term eustatic Cretaceous sea-level change: A synthesis. *Earth-Sci. Rev.* **197**, 102901 (2019). https://doi.org/10.1016/j.earscirev
15. Bottini, C. & Erba, E. Mid-Cretaceous paleoenvironmental changes in the western Tethys. *Clim. Past* **14**, 1147–1163 (2018).
16. Li, Y. et al. Radioisotopic chronology of Ocean Anoxic Event 1a: Framework for analysis of driving mechanisms. *Sci. Adv.* **10**, eadn8365 (2024).
17. Matsumoto, H. et al. Multidisciplinary evidence for synchroneity between Ontong Java Nui volcanism and early Aptian oceanic anoxic event 1a. *Sci. Adv.* **11** (9), https://doi.org/10.1126/sciadv.adt0204.
18. Leandro, C. G. et al. Astronomical tuning of the Aptian stage and its implications for age recalibrations and paleoclimatic events. *Nat. Commun.* **13** (2022).
19. Sabatino, N. et al. Mercury anomalies in upper Aptian-lower Albian sediments from the Tethys realm. *Palaeogeogr. Palaeoclimatol. Palaeoecol.* **495**, 163–170 (2018).
20. Coccioni, R. et al. Umbria-Marche Basin, Central Italy: A Reference Section for the Aptian-Albian Interval at Low Latitudes. *Sci. Drill.* **13**, 42–46 (2012).
21. Arthur, M. A., Brumsack, H. J., Jenkyns, H. C., & Schlanger, S. O. In. *Cretaceous Resources, Events and Rhythms*, 75–119. (Springer, 1990). Erba, E. et al. Environmental consequences of Ontong Java Plateau and Kerguelen Plateau volcanism. In The origin, evolution, and environmental impact of oceanic large igneous provinces. *Geol. Soc. Am. Spec. Pap.* **511**.
22. Ramos, J. M. F. et al. Anoxic Event 1b and its implications for the cause of mid-Cretaceous events: a multiproxy record. *Paleoceanogr. Paleoclimatol.* **39**(11), 1–30 (2024).
23. McAnena, A. et al. Atlantic cooling associated with a marine biotic crisis during the mid-cretaceous period. *Nat. Geosci.* **6**(7), 558–561 (2013).
24. *Overview of Cretaceous Oceanic Red Beds (CORBs): a Window on Global Oceanic and Climate Change*. Wang, C. et al. From: SEPM Society for Sedimentary Geology **91**, Cretaceous Oceanic Red Beds: Stratigraphy, Composition, Origins, and Paleoceanographic and Paleoclimatic Significance: 13–33 (2009).
25. Dummann, W. et al. The early opening of the Equatorial Atlantic gateway and the evolution of Cretaceous peak warming. *Geology* **51**(5), 476–480 (2023).
26. Savian, J. et al. The Barremian-Aptian boundary in the Poggio le Guaine core (central Italy): evidence for magnetic polarity Chron M0r and oceanic anoxic event 1a. *Geol. Soc. Am. Spec. Pap.* **524**, 57–78 (2016).
27. Sabatino, N. et al. High-resolution chemostratigraphy of the late Aptian–early Albian oceanic anoxic event (OAE 1b) from the Poggio le Guaine section (Umbria–Marche Basin, central Italy). *Palaeogeogr. Palaeoclimatol. Palaeoecol.* **426**, 319–333 (2015).
28. Coccioni, R. & Galeotti, S. The mid-Cenomanian Event: prelude to OAE 2. *Palaeogeogr. Palaeoclimatol. Palaeoecol.* **190**, 427–440 (2003).
29. Coccioni, R., & Frontalini, F. Cretaceous planktonic foraminiferal biostratigraphy of the Umbria–Marche Basin (Central Italy) In: Hart, M.B., Batenburg, S.J., Huber, B.T., Price, G.D., Thibault, N., Wagreich, M. and Walaszczyk, I. (eds) Cretaceous Project 200 Volume 2: Regional Studies. *Geological Society, London, Special Publications*, **545**(1), SP545–2023, https://doi.org/10.1144/SP545-2023-87 (2024).
30. Lamm, F. et al. Calcareous nannofossils from the Poggio le Guaine core (Umbria-Marche Basin, central Italy): Biostratigraphy and discussions on the bioevents of the Aptian–Albian interval. *Cretac. Res.* **145**, 1–19 (2023).
31. Tateo, F. et al. Orbital control on pelagic clay sedimentology: The case of the late Albian "Amadeus Segment" (central Italy). *Bull. Soc. Geol. Fr.* **171**(2), 217–228 (2020).
32. Li, Y. et al. Revised onset age of magnetochron M0r: Chronostratigraphic and geologic implications. *Geology* **51**(6), 565–570 (2023).

33. Selby, D., Mutterlose, J. & Condon, D. J. U-Pb and Re-Os Geochronology of the Aptian/Albian and Cenomanian/Turonian stage boundaries: implications for timescale calibration, osmium isotope seawater composition and Re-Os systematics in organic-rich sediments. *Chem. Geol.* **265**, 394–409 (2009).
34. Bornemann, A. et al. A first high-resolution carbon isotope stratigraphy from the Boreal (NW Germany) for the Berriasian to Coniacian interval—implications for the timing of the Aptian-Albian boundary. *Front. Earth Sci.* **11**, 1173319 (2023).
35. Coccioni, R. & Premoli Silva, I. Revised Upper Albian-Maastrichtian planktonic foraminiferal biostratigraphy and magneto-stratigraphy of the classical Tethyan Gubbio section (Italy). *Newsl. Stratigr.* **48**(1), 47–90 (2015).
36. Tiraboschi, D. et al. Origin of rhythmic Albian black shales (Piobbico core, central Italy): Calcareous nannofossil quantitative and statistical analyses and paleoceanographic reconstructions: *Paleoceanography* **24** (2009).
37. Waltham, D. Milankovitch period uncertainties and their impact on cyclostratigraphy. *J. Sediment. Res.* **85**, 990–998 (2015).
38. Li, M. et al. Tracking variable sedimentation rates and astronomical forcing in Phanerozoic paleoclimate proxy series with evolutionary correlation coefficients and hypothesis testing. *Earth Planet. Sci. Lett.* **501**, 165–179 (2018).
39. Meyers, S. R. astrochron: An R Package for Astrochronology. https://cran.r-project.org/package=astrochron (2014).
40. Meyers, S. R. & Sageman, B. Quantification of deep-time orbital forcing by average spectral Misfit. *Am. J. Sci.* **307**, 773–792 (2007).
41. Laskar., J. et al. A long-term numerical solution for the insolation quantities of the Earth. *Astron. Astrophys.* **428**, 261–285 (2004).
42. Laskar, J. et al. La2010: A new orbital solution for the long-term motion of the Earth. *Astron. Astrophys.* **532**, A89. https://doi.org/10.1051/0004-6361/201116836 (2011).
43. Laskar, J. et al. Strong chaos induced by close encounters with ceres and vesta. *Astron. Astrophys.* **532**, L4. https://doi.org/10.1051/0004-6361/201117504 (2011).
44. Zeebe, R. E. & Lourens, L. J. Geologically constrained astronomical solutions for the Cenozoic era. *Earth Planetary Sci. Lett.* **592**, 117595.https://doi.org/10.1016/j.epsl.2022.117595 (2022).
45. *The Mid-Cretaceous Organic-Rich Sediments from the Vocontian Zone of the French Southeast Basin*. Bréhéret, JG. (1994). In: Mascle, A. (eds) Hydrocarbon and Petroleum Geology of France. Special Publication of the European Association of Petroleum Geoscientists, vol 4. Springer, Berlin, Heidelberg.
46. Laskar, J. Astrochronology. In *The Geologic Time Scale 2020*, (eds. Grandstein, F. M., Ogg, J. G., Schmitz, M. D. & Ogg, G.) 139–158 (Elsevier, 2020).
47. Ma, C., Meyers, S. R. & Sageman, B. B. Theory of chaotic orbital variations confirmed by Cretaceous geological evidence. *Nature* **542**(7642), 468–470 (2017).
48. Helsley, C. E. & Steiner, M. B. Evidence for long intervals of normal polarity during the Cretaceous period. *Earth Planet. Sci. Lett.* **5**, 325–332 (1968).
49. Zhang, Y. et al. Magnetostratigraphy of U-Pb–dated boreholes in Svalbard, Norway, implies that magnetochron M0r (a proposed Barremian-Aptian boundary marker) begins at 121.2 ± 0.4 Ma. *Geology* **49** (2021).
50. Huang, C., Hinnov, L. A., Fischer, A. G., Grippo, A. & Herbert, T. Astronomical tuning of the Aptian stage from Italian reference sections. *Geology* **238**, 899–903 (2010).
51. Malinverno, A., Erba, E. & Herbert, T. D. Orbital tuning as an inverse problem: Chronology of the early Aptian oceanic anoxic event 1a (Selli Level) in the Cismon APTICORE. *Paleoceanogr. Paleocl.* **25**, PA2203 (2010).
52. Bottini, C. et al. Climate variability and ocean fertility during the Aptian Stage. *Clim. Past* **11**, 383–402 (2015).
53. Herrle, J. O. et al. High-resolution carbon isotope records of the Aptian to lower Albian from SE France and the Mazagan Plateau (DSDP Site 545): A stratigraphic tool for paleoceanographic and paleobiologic reconstruction. *Earth Planet. Sci. Lett.* **218**, 149–161 (2004).
54. Coccioni, R. & Galeotti, S. Orbitally induced cycles in benthonic foraminiferal morphogroups and trophic structure distribution patterns from the Late Albian "Amadeus Segment" (Central Italy). *J. Micropalaeontol.* **12**, 227–239 (1993).
55. Li, X. et al. Quantitative analysis of iron oxide concentrations within Aptian-Albian cyclic oceanic red beds in ODP Hole 1049C, North Atlantic. *Sediment. Geol.* **235**, 91–99 (2011).
56. Hu, X. et al. Cretaceous oceanic red beds (CORBs): Different time scales and models of origin. *Earth Sci. Rev.* **115**, 217–248 (2012).
57. Kodama, K. P. & Hinnov, L. A. Rock Magnetic Cyclostratigraphy Vol. 5 (John Wiley & Sons, 2014).
58. Mutterlose, J., Bornemann, A. & Herrle, J. O. The Aptian–Albian cold snap: Evidence for mid Cretaceous icehouse interludes. *Neues Jb. Geol. Paläontol. Abh.* **232**, 217–225 (2009).
59. Lam, A. R. et al. Diachroneity rules the mid-latitudes: a test case using Late Neogene Planktic Foraminifera across the Western Pacific. *Geosciences* **12**, 1–43 (2022).
60. Ramos, J. M. F., Savian, J. F., Franco, D. R., Figueiredo, M. F., Leandro, C. G., & Frontalini, F. Orbital tuning of short reversed geomagnetic polarity intervals in the Cretaceous Normal Polarity Superchron. *Geophys. Res. Lett.* **51**, e2024GL110530. https://doi.org/10.1029/2024GL110530. (2024).
61. Matsumoto, H. et al. Marine OS isotopic evidence for multiple volcanic episodes during Cretaceous Oceanic Anoxic Event. *Sci. Rep.* **10**, 12601 (2020).
62. Huber, B. T. & Leckie, R. M. Planktic foraminiferal species turnover across deep-sea Aptian/Albian boundary sections. *J. Foraminiferal Res.* **41**, 53–95 (2011).
63. Matsumoto, H. et al. Long-term Aptian marine osmium isotopic record of Ontong Java Nui activity. *Geology* **49**, 1148–1152 (2021).
64. Li, M., Hinnov, L. & Kump, L. Acycle: Time-series analysis software for paleoclimate research and education. *Comput. Geosci.* **127**, 12–22 (2019).
65. Herrle, J. O. et al. Mid-cretaceous High Arctic stratigraphy, climate, and oceanic anoxic events. *Geology* **43**(5), 403–406 (2015).

Acknowledgements

This study was financially supported by the Specialization and Postgraduate Program of Petrobras. J.M.F. RAMOS thanks Petrobras for Ph.D. process. The paper is a part of the projects Processamento e interpretação de dados magnetoestratigráficos do Cretáceo das Bacias Brasileiras and Magneto-cicloestratigrafia do Cretáceo na Margem Equatorial Brasileira (MEQ), both financed by Petróleo Brasileiro S.A.—Petrobras (FAURGS 8368 and 8892). J.F.S. also thanks CNPq for grants #304022/2018–7 and #311231/2021–7. D.R.F. thanks the Foundation Carlos Chagas Filho Research Support of the State of Rio de Janeiro (FAPERJ–grant #E-26/200.931/2022) and CNPq (grant #314462/2020-1). The authors sincerely thank Scientific Reports Assistant Editor Simran Gavhane and Editorial Board Member Annalisa Ferretti for their suggestions and reviews. We also thank Dr. Mike Simmons and the two anonymous reviewers for their valuable suggestions and comments during the peer-review process.

Author contributions

J.M.F.R.: conceptualization, methodology, validation, cyclostratigraphic analyses, astronomical tuning, and writing. J.F.S.: conceptualization, methodology, validation, paleomagnetic analysis, and investigation, writing, project administration, and funding acquisition. D.R.F.: methodology, cyclostratigraphic and astronomical

tuning analyses, writing. M.F.: geochemical analysis and writing. C.G.L.: cyclostratigraphic and astronomical tuning analyses, writing. F.F.: conceptualization, biostratigraphical analysis, and writing. R.C.: conceptualization, biostratigraphical analysis, and writing. H. M.: geochemical analysis and writing. N.C.: conceptualization, biostratigraphical analysis, and writing. L.R.T.: geochemical analysis and writing. L.J.: sedimentary analysis and writing. R.I.F.T.: conceptualization, methodology, validation, paleomagnetic analysis, investigation, writing, project administration, and funding acquisition.

Declarations

Competing interests

The authors declare no competing interests.

Additional information

Supplementary Information The online version contains supplementary material available at https://doi.org/10.1038/s41598-026-35714-z.

Correspondence and requests for materials should be addressed to J.M.F.R.

Reprints and permissions information is available at www.nature.com/reprints.